CRYSTAL GROWTH & DESIGN

Article

Cite This: Cryst. Growth Des. 2019, 19, 7036−7045

pubs.acs.org/crystal

Following Protein Dynamics in Real Time during Crystallization

Christian Beck,[†,‡] Marco Grimaldo,[†] Felix Roosen-Runge,[*,§] Ralph Maier,[‡] Olga Matsarskaia,[†] Michal Braun,[‡] Benedikt Sohmen,[‡,#] Orsolya Czakkel,[†] Ralf Schweins,[†] Fajun Zhang,[‡] Tilo Seydel,[*,†] and Frank Schreiber[‡]

[†]Institut Max von Laue - Paul Langevin, 71 avenue des Martyrs, 38042 Grenoble, France

[‡]Institut für Angewandte Physik, Universität Tübingen, Auf der Morgenstelle 10, 72076 Tübingen, Germany

[§]Division of Physical Chemistry, Department of Chemistry, Lund University, Naturvetarvägen 14, 22100 Lund, Sweden

Supporting Information

ABSTRACT: The process of protein crystallization from aqueous protein solutions is still insufficiently understood. During macroscopic crystal formation, occurring often on time scales from a few hours to several days, protein dynamics evolves on the molecular level. Here, we present a proof of concept and a framework to observe this evolving diffusive dynamics on the pico- to nanosecond time scale, associated with cluster or precursor formation that ultimately results in emerging crystals. We investigated the model system of the protein β-lactoglobulin in D_2O in the presence of $ZnCl_2$, which induces crystallization by electrostatic bridges. First, the structural changes occurring during crystallization were followed by small-angle neutron scattering. Furthermore, we employed neutron backscattering and spin−echo spectroscopy to measure the ensemble-averaged self- and collective diffusion on nanosecond time scales of protein solutions with a kinetic time resolution on the order of 15 min. The experiments provide information on the increasing number fraction of immobilized proteins as well as on the diffusive motion of unbound proteins in an increasingly depleted phase. Simultaneously, information on the internal dynamics of the proteins is obtained.

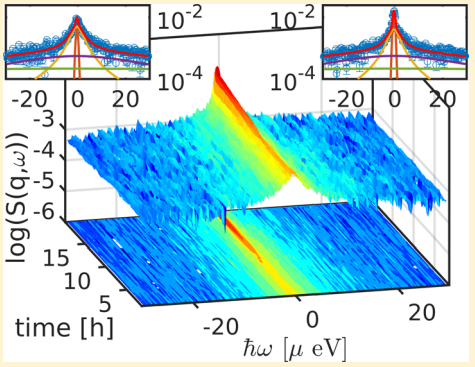

1. INTRODUCTION

Protein crystallization is of great interest due to its crucial role in the determination of protein structures in crystallography as well as for applications such as drug design.[1] Despite its importance, a fundamental understanding of the mechanisms underlying protein crystallization is still missing.[2,3] Under suitable conditions, protein crystals can grow from aqueous protein solutions. For instance, crystallization of negatively charged proteins from solution can be triggered by the presence of divalent salts such as $ZnCl_2$ or $CdCl_2$[4,5] or trivalent salts (YCl_3).[6] Appropriate conditions can induce a liquid−liquid phase separation in the system,[7,8] which might promote crystallization via two-step nucleation pathways.[6] Generally, crystal growth resulting in macroscopic crystals proceeds on different time scales[5] and may take several days.

The process of crystallization has been investigated employing various techniques such as differential scanning calorimetry,[9−11] atomic force microscopy,[12−14] transmission electron microscopy,[14,15] optical microscopy,[5,16,17] dynamic light scattering,[3,15,18] Fourier transform infrared spectroscopy,[19] small-angle X-ray scattering (SAXS),[5,15] small-angle neutron scattering (SANS),[20] and simulations.[21,22] Notably, small-angle scattering can provide information on the proteins in solution, on the crystal structure, and on protein−protein interactions during the crystallization.[5] The phase diagram and therefore also the crystallization process can be influenced by several parameters such as concentrations of both the proteins and cosolvents,[23,24] temperature,[25,26] vibrations,[27] surfaces of the sample containers,[28,29] solvents and additives[16,30−33] and electric or magnetic fields.[34] Furthermore, different purification methods or different batches of the protein in question may result in different crystallization behaviors.

While phenomenological observations and kinetic studies of the structure itself revealing both classical and nonclassical crystallization pathways[4,17,22,34−38] are relatively frequent, only a few studies are available on the molecular-level crystallization dynamics.[5,39] Studies of the diffusive dynamics of dissolved proteins and the formation of protein clusters in solution[40−48] are more common. The lack of dynamical characterization is particularly puzzling, as diffusive motions are affecting assembly in essential ways, i.e., in the case of diffusion-limited aggregation or release from frustrated local configurations.

Here, we make a proof of concept and a first step toward establishing a framework to observe and analyze the ensemble-averaged pico- to nanosecond time scale diffusive dynamics in protein solutions during crystallization in order to provide a complementary view on the process and inspire further theoretical work on the microscopic processes and dynamics.

Received: July 2, 2019
Revised: October 15, 2019
Published: October 25, 2019

DOI: 10.1021/acs.cgd.9b00858
Cryst. Growth Des. 2019, 19, 7036−7045

As a model system, we investigate aqueous (D_2O) solutions of protonated bovine β-lactoglobulin (BLG) in the presence of $ZnCl_2$.

BLG, as the major protein in the whey of ruminant species, is also interesting for applications in the food industry.[49,50]

A study of the dynamics of the proteins throughout the nucleation and crystallization process can contribute to a complete overall picture. Having verified that the crystallization process appears on suitable time scales using SANS and optical observation, we use quasi-elastic neutron backscattering spectroscopy (QENS) to access the self-dynamics of the proteins in the scattering vector range of 0.2 $Å^{-1} < q <$ 1.9 $Å^{-1}$, exploiting the prevailing incoherent scattering from their hydrogen atoms.[51] Moreover, using neutron spin−echo (NSE) spectroscopy, we access smaller q values (q = 0.082−0.1 $Å^{-1}$), where the coherent scattering dominates and therefore enables an investigation of the collective dynamics of the proteins. Before crystallization, the collective dynamics observed at the Bragg peak (q = 0.082 $Å^{-1}$)[4,5] provides information on the coordinated relaxation of concentration fluctuations with wavelengths comparable to the distances in the crystalline state. While the amount of proteins in the crystal increases, the signal at this q becomes dominated by the motion of the proteins in the crystalline state, whereas the off-peak scattering is essentially only originating from the proteins in solution throughout the process.

These neutron spectroscopy techniques thus access the evolution of the dynamics of individual proteins from their free diffusion in the supersaturated solution to their rearrangements during crystallization on different time and length scales. It is important to note that neutron scattering as a noninvasive technique is not influenced by sample turbidity (such as light scattering) and also does not lead to radiation damage, which can be a problem for X-ray scattering techniques.

Generally, we note that, although we did everything possible to ensure reproducible conditions, a complex kinetics experiment with nucleation events such as the presented one on different instruments cannot be expected to be 100% reproducible. Importantly, these neutron spectroscopic studies became only possible in the kinetic mode by significant improvements of the instrumentation in recent years.

This article focuses on the development of the experimental technique and on the data analysis and interpretation and displays a first step for exploiting systematically the dynamics throughout the crystallization process.

We emphasize that in this context certain aspects of the analysis are necessarily oversimplified, but that we believe that this helps to make the key features better visible.

2. MATERIALS AND METHODS

2.1. Sample Preparation. Bovine β-lactoglobulin (BLG, purity of 90%, L3908), $ZnCl_2$ (purity ≥99.995%, 429430), and D_2O were purchased from Sigma-Aldrich, now Merck, and used without further purification. A BLG stock solution was prepared by dissolving 200 mg of protein powder in 1 mL of D_2O (nominal concentration c_p = 200 mg/mL). The BLG stock solution was mixed with appropriate amounts of D_2O and a 100 mM $ZnCl_2$ stock solution (in D_2O) to obtain a sample with a protein concentration c_p = 100 mg/mL and a salt concentration of c_s = 35 mM. After the components were mixed, the sample was vortexed to obtain a turbid, but macroscopically homogeneous, solution. Photographs of the noncrystallized and crystallized sample are shown in the Supporting Information in Figure S1.

2.2. Small-Angle Neutron Scattering. Time-dependent SANS was performed at beamline D11[52,53] at the Institut Laue-Langevin (ILL), Grenoble, France. A freshly prepared sample was stored at 8 °C until first crystals were visible and then measured in a time series at room temperature. Neutrons with a wavelength of λ = 6 Å with $\Delta\lambda/\lambda$ = 9% were used to measure for 2 min per run at a sample-to-detector distance of 2 m (with an incident beam collimation distance of 5.5 m) covering a q-range from 0.03 $Å^{-1} < q <$ 0.33 $Å^{-1}$. The scattering vector is defined by

$$q = \frac{4\pi \sin\theta}{\lambda} \quad (1)$$

with a scattering angle 2θ. A rectangular neutron beam of 10 mm height and 7 mm width was used to illuminate the samples which were filled into Hellma quartz cuvettes of 1 mm path length. The scattering intensity was recorded with a ^{3}He MWPC CERCA detector with 256 × 256 pixels of 3.75 mm × 3.75 mm size. The two-dimensional scattering data were corrected pixel by pixel according to standard routines and then azimuthally averaged to obtain one-dimensional scattering curves as presented in Figure 1. For the data

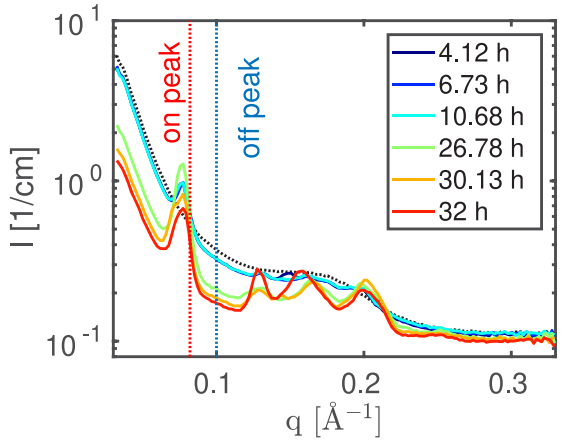

Figure 1. SANS measurements of two different samples with the same concentration. The black dotted line shows the SANS profile of a noncrystallizing sample prepared at room temperature. Solid lines show the time dependence of a second sample which was followed after macroscopic crystals were already visible in the cuvette which was stored at 8 °C. The red and blue dotted vertical lines represent the q-values at which the NSE measurements were performed. All SANS measurements were performed at 20 °C. These data represent the best time resolution currently available for this sample condition, evidencing the course of crystallization on time scales of several hours.

reduction, the LAMP software available at the ILL was employed. Light water (H_2O, 1 mm path-length) served as a secondary intensity calibration standard. Data were put on absolute scale by using the differential scattering cross section of H_2O (0.983 cm^{-1} for λ = 6 Å).

2.3. Quasi-Elastic Neutron Backscattering. For the quasi-elastic neutron backscattering (QENS) measurements, the sample was filled into a double-walled aluminum cylinder (23 mm outer diameter, 0.15 mm gap, i.e. difference between inner and outer radius), sealed against a vacuum and inserted into the instrument at T = 7 °C for the measurement.[54] The experiment was carried out using the cold neutron backscattering spectrometer IN16B at the ILL.[55] The sample was inserted into a standard orange cryofurnace mounted inside the evacuated secondary spectrometer chamber. The instrument was used with unpolished Si(111) crystal monochromator and analyzers and a vertically position-sensitive multidetector (PSD) consisting of 16 ^{3}He detector tubes covering a scattering vector range of 0.57 $Å^{-1} < q <$ 1.94 $Å^{-1}$. In addition, two small-angle detectors with a slightly lower energy resolution (due to a small angular deviation from backscattering) were placed at q = 0.19 $Å^{-1}$ and 0.29 $Å^{-1}$. An energy transfer range of $-30\ \mu eV < \hbar\omega < 30\ \mu eV$ was detectable in the so-

DOI: 10.1021/acs.cgd.9b00858
Cryst. Growth Des. 2019, 19, 7036−7045

called inverse geometry by Doppler-shifting the incident monochromatic neutrons using an AEROLAS Doppler drive operating with a sinusoidal velocity profile with an amplitude of 75 mm and maximum velocity of 4.5 m/s. The flux at the sample was optimized by a phase space transformer (PST) chopper disk,[56] carrying graphite mosaic crystals at its circumference and spinning at 7100 rpm during the experiment, corresponding to a crystal velocity of 243 m/s.

During the entire backscattering experiment, we recorded 15 min frames at full energy range. By using a running average, the raw data were binned to obtain spectra which were collected over 3 h with a time resolution of 15 min. Data reduction and fits were carried out using MATLAB R2017a (The MathWorks, Inc.). We normalized the measured intensities by the incident neutron flux and detector efficiency obtained from the vanadium measurement, and we subtracted an empty can signal from the protein solution spectra. Since the spectra collected are based on counting events, its errors are given by Poisson statistics.

2.4. Neutron Spin−Echo Spectroscopy. A sample with identical concentrations was prepared and measured using the neutron spin−echo spectrometer IN11 at the ILL.[54,57] The sample was filled into a 1 mm quartz cuvette and measured at $T = 7$ °C with a wavelength of $\lambda = 8$ Å iterating between the scattering angles 6° and 7.3°, covering the scattering vectors $q_{Bragg} = 0.082$ Å^{-1} and $q_{off} = 0.1$ Å^{-1}. Measurements were only performed at these scattering vectors to focus on the time dependence of the crystal growth.

Since the sample did not crystallize homogeneously over the entire cuvette, the sample was partially shielded with cadmium (around 41 h after the sample preparation) to focus on the crystal growth once crystals were visible by eye. The resolution functions of the instrument were determined for the different experimental conditions using the elastic scattering of graphite, measured with the exact same Cd-mask as the protein sample. Each Fourier time point was measured for 45−90 s, resulting in a time resolution of around 80 min per scattering angle q. The data were normalized by the instrument resolution function and further analyzed with MATLAB.

3. RESULTS AND DISCUSSION

3.1. Structural Characterization. SANS measurements were performed to investigate the time the sample needs to crystallize and to determine Bragg peak positions. Figure 1 shows the time-dependent scattering signal of the sample. A sample prepared and measured at room temperature did not crystallize and served as a noncrystallizing reference (black dotted line). By decreasing the temperature to $T = 8$ °C, crystal growth could be triggered in a second sample. Once crystals were visible, they continued growing at room temperature and were measured by SANS. During the crystallization process, the overall scattering intensity decreases owing to the decrease of protein clusters in solution. Upon crystal formation Bragg peaks appear, which are used for the dynamic measurements later, whose intensity increases as the crystallization process evolves.

3.2. Model of the Scattering Function for Backscattering describing the Self Diffusion. When hydrogenated proteins are measured in deuterated solvents, the incoherent scattering from hydrogen dominates in the q-range investigated with IN16B. In contrast to the coherent scattering containing structural information investigated in the previous section, the short-time self-diffusion is investigated with incoherent QENS.[58]

In a crystallizing sample, at least two protein populations contribute to the scattering function: immobile proteins inside and mobile ones outside of the crystals. Besides, salt-induced[4,5,44,59] as well as crowding-induced[42,47] oligomeric populations may be present. While the global diffusion of proteins in crystals (as well as those in very large aggregates, diffusing so slowly that the energy transfers cannot be detected with the given energy resolution, see section 3.3) should be negligible, we expect the "free" proteins to be well observable within the accessible time scale. Moreover, internal motions contribute to the recorded scattering function as well. In principle, internal dynamics could be different in crystals and in solution. Although a change of fast vibrational dynamics was observed by Raman spectroscopy upon lysozyme crystallization,[60] nuclear magnetic resonance (NMR) studies suggest that differences on a pico- to nanosecond time scale are absent or very limited.[61,62] Hence, in order to keep the model as simple and robust as possible, i.e., to reduce the number of free parameters, we model the scattering function $S(q, \omega)$ as a sum of the contributions from nondiffusing proteins in crystals or large aggregates and diffusing proteins in solution with the same internal dynamics:

$$\begin{aligned} S(q,\omega) = \mathcal{R}(q,\omega) \otimes \{\beta(q)\cdot & \\ & [A_c[A_0(q)\delta(\omega) + (1 - A_0(q))\mathcal{L}_\Gamma(\omega)] \\ & + (1 - A_c)[A_0(q)\mathcal{L}_\gamma(\omega) + (1 - A_0(q))\cdot \\ & \mathcal{L}_{\gamma+\Gamma}(\omega)]] + \beta_{D_2O}\mathcal{L}_{\gamma D_2O}(\omega)\}. \end{aligned} \quad (2)$$

q denotes the scattering vector and $\hbar\omega$ is the energy transfer. We note that the assumption of identical internal dynamics of proteins in crystals and in solution may lead to systematic errors. In contrast, allowing for (slightly) different dynamics as well as considering additional contributions from protein clusters would render the fit ill-posed. We therefore prefer a simplified model. In eq 2, A_c and $(1 - A_c)$ denote the fraction of nondiffusing and diffusing proteins, respectively, and $\delta(\omega)$ is a delta function accounting for immobile proteins. $\mathcal{L}_{\{...\}}$ denote Lorentzian functions accounting for diffusive (global and internal) dynamics with the index to this symbol denoting the respective half-width at half-maximum. In particular, the line width γ accounts for the averaged global diffusion of monomeric and dimeric proteins as well as of small protein clusters in solution, whereas Γ describes the average internal dynamics. $\beta(q)$ is a scaling factor, while the so-called elastic incoherent structure factor (EISF) $A_0(q)$ provides information on the geometry of confinement of atoms within the protein.[63] Finally, the term $\beta_{D_2O}\mathcal{L}_{\gamma D_2O}(\omega)$ accounts for the contribution of D_2O and is fixed during the fit, as explained in ref 64 and $\mathcal{R}(q, \omega)$ represents the resolution function of IN16B determined from the spectrum of a vanadium standard (width ≈ 0.9 μeV full width at half-maximum). In the fit algorithm, $\mathcal{R}(q, \omega)$ is described analytically by a sum of two Gaussian functions, and the convolution $\mathcal{R}(q, \omega) \otimes \{...\}$ is carried out analytically, yielding $\mathcal{R}(q, \omega) \otimes \delta(\omega) = \mathcal{R}(q, \omega)$ and Voigt functions consisting of $\mathcal{R}(q, \omega)$ and $\mathcal{L}_{\{...\}}$.

In a first step, the parameters $\beta(q)$, $A_0(q)$, γ, and Γ are fitted q-wise, while A_c is set as a global, q-independent parameter. The errors of the fit results represent the 95% confidence bounds of the fit based on the inverse Jacobian matrix. Two examples of a fitted spectrum (first and last spectrum of the time dependent measurement) are shown in the insets of Figure 2 with the main figure showing the time dependence of the scattering signal at $q = 1.48$ Å^{-1}. Already in the raw data, a reduction of the overall spectral width and an increase of the elastic contribution with time are visible. The widths γ

DOI: 10.1021/acs.cgd.9b00858
Cryst. Growth Des. 2019, 19, 7036−7045

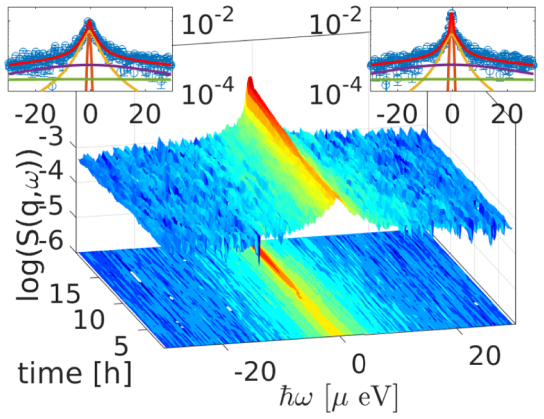

Figure 2. Time dependence of the backscattering signal at q = 1.48 Å^{-1}. The increase of the elastic contribution with time can already be seen in the raw data. The two insets show fits (red line) at the same q = 1.48 Å^{-1} for the first (left) and last (right) collected spectra. Brown, yellow, purple, and green lines represent contributions of immobile proteins, global and internal diffusion and D_2O contribution, respectively. During the whole measurement, the sample was kept at T = 280 K.

obtained from a fit of eq 2 are plotted as a function of q^2 in Figure 3.

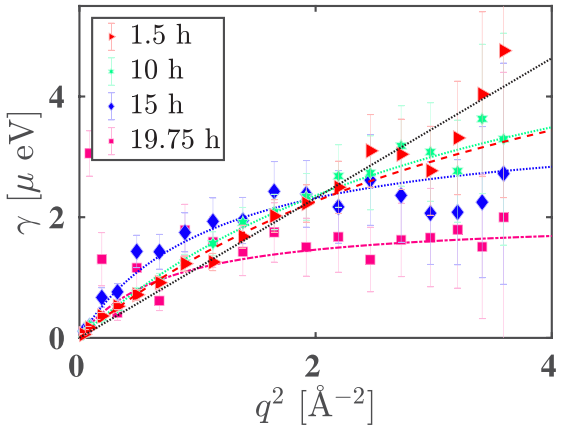

Figure 3. Lorentzian line width γ (symbols) vs q^2 characterizing the global diffusion obtained from the fits of eq 2 to the backscattering spectra at four different times t after sample preparation. The fits with eq 3 (lines) describe a jump-diffusion. At t = 1.5 and 10 h, γ deviates slightly from a straight line, which would indicate free Brownian diffusion, whereas at longer times the deviation from $\gamma \propto q^2$ is much more pronounced, and a jump-diffusion-like behavior is clearly recognizable.

The red triangles in Figure 3 corresponding to the sample 1.5 h after preparation deviate slightly from a straight line (shown as black dotted line). We use a well-established formula to fit this apparent signature in q, as described by the Singwi and Sjölander jump-diffusion model[65]

$$\gamma = \frac{Dq^2}{1 + \tau Dq^2} \tag{3}$$

where D is the jump-diffusion coefficient and τ denotes the residence time in the trapped state. The trend obtained from eq 3 becomes even more pronounced at longer times, as noticeable from the flattening of γ at higher q. Three reasons may explain the deviations of γ at low q-values. First, because of the design of the instrument, the first two detectors have a broader energy resolution than the other 16 detectors. Second, the lowest detector covers the Bragg peak visible in Figure 1. In the presence of crystals, the scattering signal at this detector therefore contains significant coherent contributions which are not accounted for in the model. Third, at low q, quasi-elastic broadenings are very small and close to the energy resolution and, as shown in section 3.3, at longer times the contribution of diffusing proteins decreases, such that even small inaccuracies in the analytical description of $\mathcal{R}(q, \omega)$ may have a large influence on the fitting parameters.

Having verified that the q dependence of γ can be described by eq 3, we impose this q-dependence in eq 2 on D and τ to reduce their errors. Hence, we now fit $S(q, \omega)$ with A_c, D, and τ as global parameters with the two latter parameters describing the global diffusion according to eq 3. This slightly different procedure does not significantly change the values of any parameter (see Supporting Information, Figure S3 and Figure S4) but, as expected, increases the accuracy of A_c, D, and τ.

As shown in the Supporting Information in Figure S5, the global diffusion coefficient exceeds the dilute limit, i.e., the theoretical diffusion coefficient at infinite dilution calculated based on the protein structure (see Figure S5 in the Supporting Information) or the value extrapolated based on values determined by PFG-NMR ($D = 4.82 \frac{Å^2}{ns}$,[66] rescaled to T = 7 °C according to the Stokes−Einstein relation). Since the internal dynamics is assumed to be the same for proteins in solution and in the crystals, it should not change during the transition from a solvated protein to a crystal. The parameters should therefore also remain constant over time. Fixing the internal dynamics based on the first binned QENS spectrum leads to an apparent global diffusion coefficient which approaches the dilute limit but does not exceed it. This indicates that the Lorentzian function describing the global dynamics can no longer be unambiguously separated from the one describing the internal dynamics on the limited energy range investigated if all parameters have to be determined by the fit.

The results of this third fit with q-global fit parameters and fixed internal dynamics will be shown and discussed in the following sections.

3.3. Fraction of Immobilized Proteins. The coefficient A_c in eq 2 describes the fraction of nondiffusing proteins on the time scale accessible (up to a few nanoseconds) such as crystals and big aggregates and precursors. In fact, after opening the sample holder many crystals were found. However, the opening was possible only several hours after the experiment because of radiation protection regulations. The system might thus have first developed amorphous aggregates, which eventually crystallized (as it happens for nonclassical crystallization[4−6]).

Figure 4 shows A_c as a function of time. The model indicates that ∼10% of the proteins in the sample are immobile in the first analyzed spectra, although they are not part of crystals, pointing to cluster formation immediately after the sample preparation, which is also supported by the turbidity of the sample after sample preparation (see Figure S1 in the Supporting Information). After about 7 h, the fraction of nondiffusing proteins starts to increase, first slowly, then more quickly, going up to ∼65%. Hence, because of the

DOI: 10.1021/acs.cgd.9b00858
Cryst. Growth Des. 2019, 19, 7036−7045

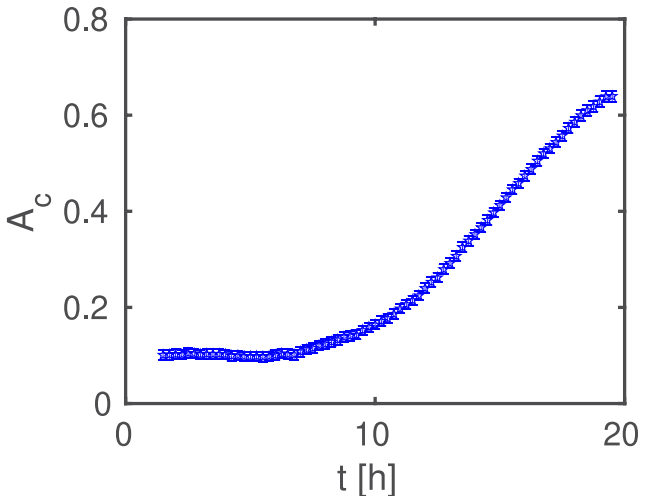

Figure 4. Fraction of immobile proteins A_c as a function of time obtained from the QENS spectra applying fits based on eq 2 with fixed internal dynamics.

crystallization process, the volume fraction of proteins in solution

$$\varphi_{free} = (1 - A_c)c_p\vartheta/(1 + c_p\vartheta) \quad (4)$$

decreases to $\varphi \simeq 0.025$, corresponding to a free protein concentration of $c_p^{free} = \frac{\varphi}{\vartheta - \vartheta\varphi} \simeq 34\frac{mg}{mL}$, calculated with a specific volume of $\vartheta = 0.75\ \frac{mL}{g}$.[66]

Given the experimental data, it cannot yet be determined if the clusters observed at the beginning are precursors of the crystallites or if they serve as protein reservoirs which redissolve again during the crystallization process.[5]

Applying eq 2 to pure protein solutions, A_c as well as τ are zero within the error bars as expected (see Supporting Information, Figure S6). Other protein systems with concentrations up to $c_p = 500\ \frac{mg}{mL}$ have already been investigated previously,[45] still showing quasi-elastic contributions and no significant elastic contribution.

3.4. Global Diffusion. As explained in section 3.2, eq 3 is imposed on the global fit of $S(q, \omega)$ and the internal dynamics is fixed based on the first run. The obtained diffusion coefficients D and residence times τ are plotted as a function of time in Figure 5, panels a and b, respectively. The two trends are very similar to the one of A_c: for about 10 h, D and τ remain almost constant and then increase up to $D \simeq 5$ Å^2/ns and $\tau \simeq 0.3$ ns, respectively. More systematic measurements at different sample conditions are necessary to confirm and to extract reliable information on the time dependence of D and of τ, such as the small peak between 7 and 10 h and the shoulder at ∼14 h, respectively, and to link them to the crystallization progress.

Several effects influence the global diffusion. First, since the amount of proteins bound in crystals increases, the volume fraction of proteins, which diffuse freely in solution, decreases over time. As shown in several previous studies, this effective dilution leads to an increasing diffusion coefficient up to the dilute limit[42,43,46,47] ($D = 5.95\ \frac{Å^2}{ns}$). With increasing global diffusion coefficients, the separation of internal and global diffusion becomes difficult due to the limited dynamic range of the instrument. To obtain reasonable values, this cross-talk in

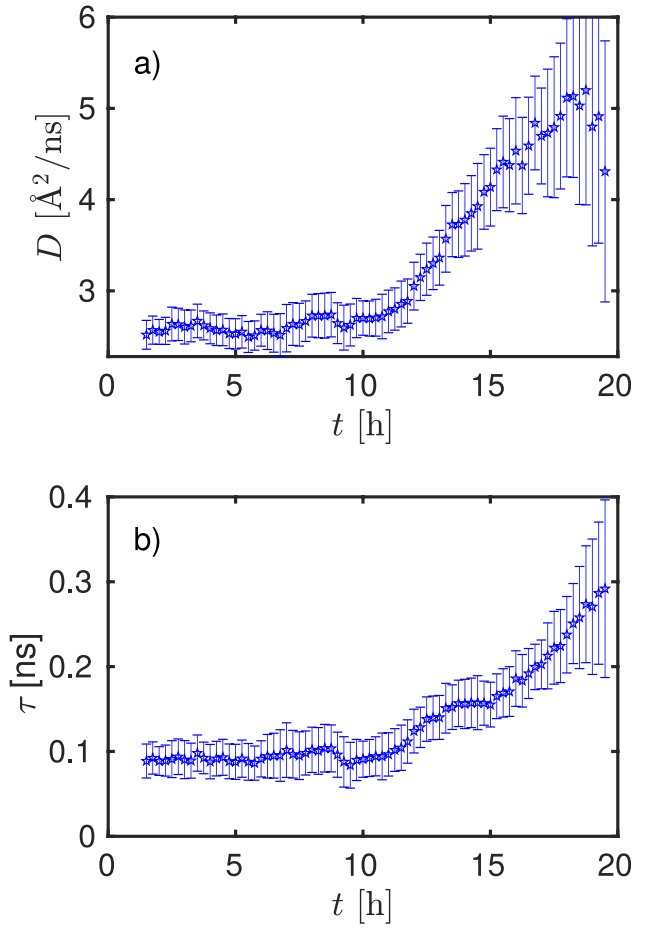

Figure 5. Time dependence of the parameters characterizing the averaged global dynamics from the proteins in solution determined from the global fits of eq 2 with fixed internal dynamics and eq 3 describing the global diffusion as a function of time. Figure 5a displays the global short-time self-diffusion coefficient D as a function of time. For long times, the observed diffusion coefficient approaches the dilute limit of monomers (see also Figure S5). Figure 5b shows the time dependence of the residence time τ.

the fit is reduced by fixing the width for the internal dynamics. Second, the presence of multivalent ions in solution can lead to a salt-dependent slowing down of the apparent diffusion coefficient.[44,59] Since the concentration of salt ions in the solution could not be measured during the experiment and the influence of $ZnCl_2$ on the short-time self-diffusion of BLG has not been studied systematically, the fraction of immobile proteins, A_c, cannot be quantitatively linked to the diffusion coefficient in a straightforward fashion. Nevertheless, although a quantitative connection cannot be established, the general trend can be compared directly. Different plots using different axes are displayed in the Supporting Information in Figure S2. We note that the jump-diffusion process observed might also be linked to low statistics in contributions of the scattering function due to the low protein concentration in solution.

3.5. Geometry of Confined Motions. Figure 6 shows the q-dependence of the EISF obtained from the fits with A_c as the only q-independent parameter for different times. Clearly, the EISF does not change much throughout the process, which gives an *a posteriori* justification for the same internal dynamics assumed for the two populations. The q-dependence of the EISF is described using a model containing a fraction p of

DOI: 10.1021/acs.cgd.9b00858
Cryst. Growth Des. 2019, 19, 7036−7045

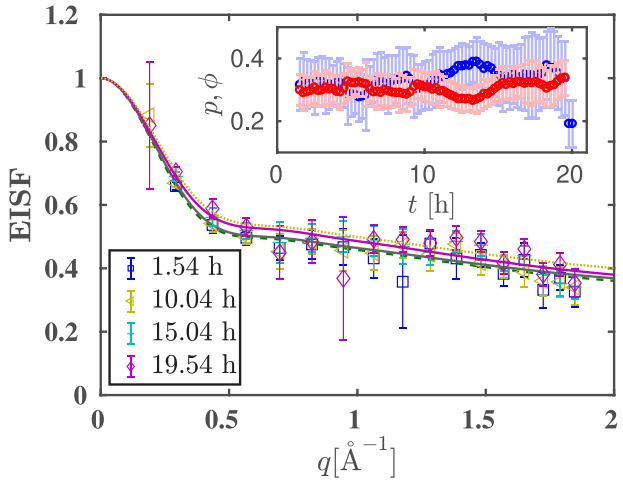

Figure 6. Time dependence of the EISF $A_0(q)$ as a function of q describing the dynamics on a molecular length scale as obtained from the QENS spectra by fitting eq 2 with free internal dynamics. Although a significant fraction of the proteins arrange into immobile assemblies, the EISF does not change significantly, which validates a posteriori the assumption that the internal dynamics does not change significantly between the different global arrangements. The time dependence of the different fit parameters (red: p ; blue: Φ) of the EISF from eq 7 are shown in the inset. Within the errors, the parameters are constant in time.

nondiffusive contributions, three-site jump-diffusion processes $A_{3-j}(q)$ as well as diffusion in an impermeable sphere $A_{sph}(q)$[43,45,47] for each time-step:

$$A_{3-j} = \frac{1 + 2j_0(qa_m)}{3} \tag{5}$$

$$A_{sph} = \left| 3\frac{j_1(qR)}{qR} \right|^2 \tag{6}$$

$$A_0 = p + (1 - p)[\Phi A_{3-j} + (1 - \Phi)A_{sph}] \tag{7}$$

with the nth order spherical Bessel function j_n and the jump distance of H atoms in methyl groups a_m = 1.715 Å. While Figure 6 displays the q dependence of the EISF, the inset shows the time dependence of the fit parameters p and Φ of eq 7. The parameters agree within the error bars with the values of pure BLG solutions.[47] This observation also supports the assumption that the geometry of the confined motions and the internal dynamics is, to a good approximation, independent of whether the proteins are in solution or parts of aggregates or crystals.

3.6. Model for the Scattering Function in NSE. Similar to SANS, neutron spin−echo measurements can access the coherent scattering containing structural information. At different scattering vectors, the kinetics of different components involved in the crystallization process can be followed.[5] The dynamics of the same components during the crystallization process can be investigated via NSE measurements sampling the same scattering vectors. The red and blue vertical dashed lines in Figure 1 represent the q-values at which the NSE measurements are performed.

We emphasize that in the beginning, in the absence of crystals, the same information about the dynamics is obtained from the scattering functions collected at the different q-values. Only in the presence of crystals, the scattering function measured at q_{Bragg} and at q_{off} contains different dynamical contributions.

Selected examples of the intermediate scattering function $F(q, t)$ measured with NSE on and off the Bragg peak are shown in Figure 7. Clearly, the intermediate scattering function

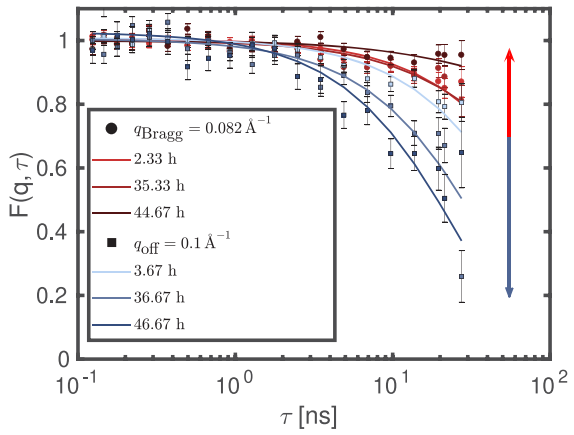

Figure 7. Examples of the intermediate scattering functions measured at IN11 from BLG c_p = 100 $\frac{mg}{mL}$ and c_s = 35 mM. Red circles and blue squares show data measured on and off the Bragg peak, respectively. The time steps are coded by the brightness of the points as shown in the legend. Solid lines show the fit results.

on-peak (q_{Bragg} = 0.082 Å^{-1}) flattens while crystals grow, indicating that the average diffusion on this length scale decreases, while off-peak (q_{off} = 0.1 Å^{-1}), the dynamics becomes faster, consistent with the results from backscattering.

As a simple model, we assume only two different contributions to the scattering function. By describing the off-peak intermediate scattering function via

$$F(q, t) = \exp[-D_c^f(q)q^2] \tag{8}$$

we describe mainly the collective diffusion of the fraction of proteins, which are in either monomeric state or in clusters. Hence, in eq 8, $D_c^f(q)$ denotes the collective diffusion coefficient of free proteins in solution. At q_{Bragg}, instead, the intermediate scattering function is

$$F(q, t) = A_c \exp[-D_c^c(q)q^2] + (1 - A_c) \exp[-D_c^f(q)q^2] \tag{9}$$

where $D_c^f(q)$ denotes again the collective diffusion coefficient of proteins in solution, $D_c^c(q)$ is the diffusion coefficient of crystallizing or crystallized proteins, and A_c is the fraction of proteins in crystals. If we furthermore assume that $D_c^f(q) = D_c^f$ is a q-independent parameter, we can first fit eq 8 at q_{off} and then use D_c^f in eq 9, leaving A_c and D_c^c as free parameters. The fits with eqs 8 and 9 are shown in Figure 7. The data thus seem to be consistent with this simple model.

3.7. Collective Dynamics Studied at Different *q*. We note that differences at the Bragg peak position were visible only several hours after crystals were observable by eye. If only few crystals are present at the beginning of the process, discrete Bragg reflections are visible. The powder average might therefore not be fulfilled at the beginning of the crystallization process. Since the detector of IN11A only covers a small fraction of the total solid angle, Bragg reflections might have been initially positioned outside of the detector area of IN11A and then moved into the detection range.

DOI: 10.1021/acs.cgd.9b00858
Cryst. Growth Des. 2019, 19, 7036−7045

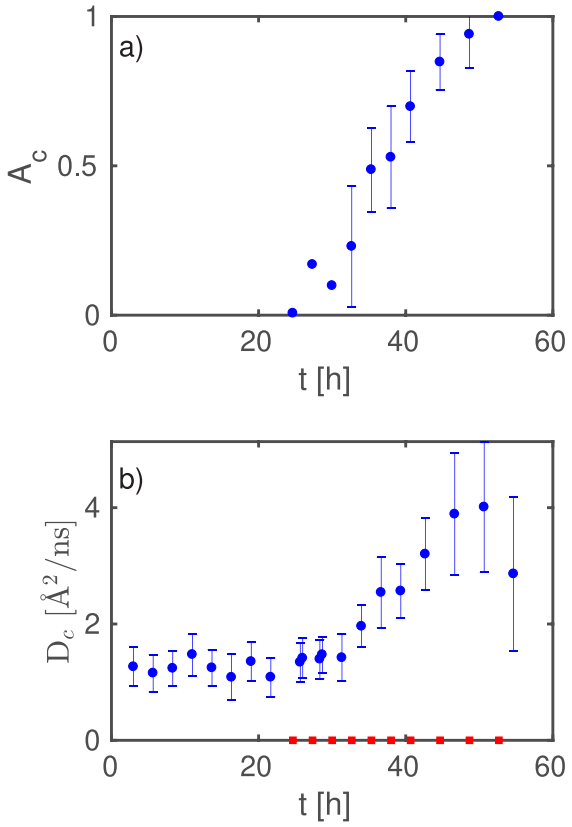

Figure 8. Results of the analysis of the neutron spin−echo data based on eq 8 and 9 shown in Figure 7. (a) The time dependence of the fraction of proteins within the crystals and of the diffusion coefficient of the dissolved proteins in solution agrees qualitatively with the results obtained from the QENS analysis shown in Figures 4 and 5. (b) The obtained diffusion coefficients off-peak and on-peak are shown in blue circles and red squares, respectively. While the diffusion coefficient of the proteins in solution observed with NSE increases similarly to the one observed with QENS (see Figure 5a), no dynamics could be extracted from the proteins in the crystals.

Figure 8a,b shows A_c and D_c as functions of time obtained from fitting eq 8 and eq 9 to data measured off-peak at q_{off} = 0.1 Å^{-1} and on peak (q_{Bragg} = 0.08 Å^{-1}), respectively. Similar to the self-diffusion coefficient, the collective diffusion coefficient D_c^f also increases in parallel with A_c, which is consistent with a depletion effect. This observation also confirms that off-peak we obtain essentially only the signal from proteins in solution. Figure 8b also shows the collective diffusion coefficient D_c^c (red squares). We do not see any additional dynamics on the length scale of the Bragg peak within the time scales studied. With longer time scales as well as with more scattering vectors measured, a better separation between the different contributions would be possible. Given the negligible values of D_c^c, the model can be simplified using an apparent flat background within the correlation times presently accessible. Future NSE measurements with higher Fourier times might access the corresponding diffusive dynamics, which would then be described by the second exponential function.

4. CONCLUSIONS

We have presented a proof of concept and an analytical framework to investigate the process of protein crystallization in solution, proceeding on a time scale of several hours, by measuring the short-time diffusive dynamics of proteins in solution and in aggregates and crystals on different time scales such as on the nanosecond time scale with QENS and on longer time scales with NSE. By combining neutron spin−echo and backscattering spectroscopy, we access both the collective dynamics on the Bragg peak and the dynamics in the liquid phase at other scattering vectors. Because of the high scattering vector, corresponding to a nanometer observation length scale, and the absence of polarization analysis, backscattering accesses the self-diffusion of the proteins via their prevailing incoherent scattering. Notably, both experiments corroborate an onset of a slowly and continuously growing fraction of proteins that are immobile during the experimental observation or coherence time of a few nanoseconds in the backscattering experiment and a few tens of nanoseconds in the neutron spin−echo experiment. This immobility may be associated with emerging protein aggregates or later with crystallites forming in the sample. In parallel, a decreasing protein monomer concentration in the depleted phase manifests itself by monomer diffusion coefficients that increase as crystallization proceeds. This increase of the observable monomer center-of-mass diffusion can be partially explained by the decrease of the crowding effect by the freely diffusing proteins. Measuring more scattering vectors with NSE and up to higher energy transfers with QENS will allow in future studies to separate additional contributions such as those from aggregates and will thus reveal more information about the crystallization pathways and the dynamical properties of the different species involved. The backscattering experiment simultaneously accesses the superimposed internal diffusive motions within the proteins. These motions seem to be nearly unaffected by the crystallization within the precision currently achievable, but may be further studied with improved setups. Our framework opens the perspective to systematically study the dynamics of protein crystallization of numerous protein solution samples. Given the time-dependent changes of the sample, the statistics of the scattering data is flux-limited. Accessing several scattering vectors simultaneously using future NSE instruments and using future neutron sources with higher peak neutron fluxes or measuring slower crystallizing samples will offer access to the dynamics of the proteins in the different phases of the (multistep-) crystallization processes with higher accuracy. Future wide-angle NSE instruments may also permit the study of the formation of single large crystals. The influence of different protein and salt concentrations on the kinetic changes of the diffusion can be systematically investigated in future studies. Such systematic studies will contribute to a better fundamental understanding of crystallization pathways, which will help to address the bottleneck of obtaining diffraction-quality crystals for applications in structural biology.

■ ASSOCIATED CONTENT

Supporting Information

The Supporting Information is available free of charge on the ACS Publications website at DOI: 10.1021/acs.cgd.9b00858.

Photographs of the sample measured with NSE, comparisons between different fit approaches of the QENS spectra as well as fit results of eq 2 of the QENS spectra without salt (PDF)

■ AUTHOR INFORMATION

Corresponding Authors

*(F.R.-R.) E-mail: felix.roosen-runge@fkem1.lu.se.

DOI: 10.1021/acs.cgd.9b00858
Cryst. Growth Des. 2019, 19, 7036−7045

*(T.S.) E-mail: seydel@ill.eu.

ORCID

Christian Beck: 0000-0001-7214-3447
Marco Grimaldo: 0000-0002-3772-7137
Felix Roosen-Runge: 0000-0001-5106-4360
Olga Matsarskaia: 0000-0002-7293-7287
Ralf Schweins: 0000-0001-8078-2089
Fajun Zhang: 0000-0001-7639-8594
Tilo Seydel: 0000-0001-9630-1630

Present Address

#(B.S.) Institute of Physical Chemistry, Universität Freiburg, Albertstraße 23a, 79104 Freiburg, Germany

Notes

The authors declare no competing financial interest.

The neutron data are permanently curated by the ILL and accessible via DOI: 10.5291/ILL-DATA-04-760 (Backscattering data and NSE)[54] and DOI: 10.5291/ILL-DATA.9-13-620 (SANS data).[53]

■ ACKNOWLEDGMENTS

This work was supported in part by the DFG and the ANR (Contract No. ANR-16-CE92-0009-01) and the Knut and Alice Wallenberg Foundation (Project Grant KAW 2014.0052). C.B. acknowledges the support by a studentship cofunded by the ILL and the University of Tübingen. We thank Ingo Hoffmann, Andrea Sauter, and Stefano da Vela for fruitful discussions and the PSCM (Grenoble) for sharing their laboratory resources. The open access fee was covered by FILL2030, a European Union project within the European Commission's Horizon 2020 Research and Innovation programme under grant agreement No. 731096.

■ REFERENCES

(1) Gunton, J.; Shiryayev, A.; Pagan, D. *Protein Condensation: Kinetic Pathways to Crystallization and Disease*; Cambridge University Press, 2007.

(2) Profio, G. D.; Curcio, E.; Drioli, E. *Encyclopedia of Industrial Biotechnology*; American Cancer Society, 2010; pp 1−22.

(3) Schubert, R.; Meyer, A.; Baitan, D.; Dierks, K.; Perbandt, M.; Betzel, C. Real-Time Observation of Protein Dense Liquid Cluster Evolution during Nucleation in Protein Crystallization. *Cryst. Growth Des.* **2017**, *17*, 954−958.

(4) Sauter, A.; Roosen-Runge, F.; Zhang, F.; Lotze, G.; Feoktystov, A.; Jacobs, R. M. J.; Schreiber, F. On the Question of Two-Step Nucleation in Protein Crystallization. *Faraday Discuss.* **2015**, *179*, 41−58.

(5) Sauter, A.; Roosen-Runge, F.; Zhang, F.; Lotze, G.; Jacobs, R. M. J.; Schreiber, F. Real-Time Observation of Nonclassical Protein Crystallization Kinetics. *J. Am. Chem. Soc.* **2015**, *137*, 1485−1491.

(6) Sauter, A.; Oelker, M.; Zocher, G.; Zhang, F.; Stehle, T.; Schreiber, F. Nonclassical Pathways of Protein Crystallization in the Presence of Multivalent Metal Ions. *Cryst. Growth Des.* **2014**, *14*, 6357−6366.

(7) Vliegenthart, G. A.; Lekkerkerker, H. N. W. Predicting the gas-liquid critical point from the second virial coefficient. *J. Chem. Phys.* **2000**, *112*, 5364−5369.

(8) Zhang, F.; Roosen-Runge, F.; Sauter, A.; Wolf, M.; Jacobs, R. M. J.; Schreiber, F. Reentrant condensation, liquid−liquid phase separation and crystallization in protein solutions induced by multivalent metal ions. *Pure Appl. Chem.* **2014**, *86*, 191−202.

(9) Liu, T.; Mo, Z.; Wang, S.; Zhang, H. Nonisothermal Melt and Cold Crystallization Kinetics of Poly(aryl ether ether ketone ketone). *Polym. Eng. Sci.* **1997**, *37*, 568−575.

(10) Lorenzo, A. T.; Arnal, M. L.; Albuerne, J.; Müller, A. J. DSC Isothermal Polymer Crystallization Kinetics Measurements and the Use of the Avrami Equation to Fit the Data: Guidelines to Avoid Common Problems. *Polym. Test.* **2007**, *26*, 222−231.

(11) Kolstad, J. J. Crystallization Kinetics of Poly(L-lactide-co-meso-lactide). *J. Appl. Polym. Sci.* **1996**, *62*, 1079−1091.

(12) Land, T. A.; Malkin, A. J.; Kuznetsov, Y.; McPherson, A.; De Yoreo, J. J. Mechanisms of Protein Crystal Growth: An Atomic Force Microscopy Study of Canavalin Crystallization. *Phys. Rev. Lett.* **1995**, *75*, 2774−2777.

(13) Bolos, V. J.; Benitez, R.; Eleta-Lopez, A.; Toca-Herrera, J. L. A Probabilistic Model for Crystal Growth Applied to Protein Deposition at the Microscale. *Materials* **2019**, *12*, 479.

(14) Tao, J.; Nielsen, M. H.; De Yoreo, J. J. Nucleation and Phase Transformation Pathways in Electrolyte Solutions Investigated by in situ Microscopy Techniques. *Curr. Opin. Colloid Interface Sci.* **2018**, *34*, 74−88.

(15) Zhang, J.; Wang, X.; Zhou, K.; Chen, G.; Wang, Q. Self-Assembly of Protein Crystals with Different Crystal Structures Using Tobacco Mosaic Virus Coat Protein as a Building Block. *ACS Nano* **2018**, *12*, 1673−1679.

(16) Garcia-Ruiz, J. M.; Moreno, A. Investigations on Protein Crystal Growth by the Gel Acupuncture Method. *Acta Crystallogr., Sect. D: Biol. Crystallogr.* **1994**, *50*, 484−490.

(17) Lin, C.; Zhang, Y.; Liu, J. J.; Wang, X. Z. Study on Nucleation Kinetics of Lysozyme Crystallization. *J. Cryst. Growth* **2017**, *469*, 59−64.

(18) Chayen, N. E.; Saridakis, E. Protein Crystallization: From Purified Protein to Diffraction-Quality Crystal. *Nat. Methods* **2008**, *5*, 147−153.

(19) Huang, W.; Krishnaji, S.; Tokareva, O. R.; Kaplan, D.; Cebe, P. Tunable Crystallization, Degradation, and Self-Assembly of Recombinant Protein Block Copolymers. *Polymer* **2017**, *117*, 107−116.

(20) Heigl, R. J.; Longo, M.; Stellbrink, J.; Radulescu, A.; Schweins, R.; Schrader, T. E. Crossover from a Linear to a Branched Growth Regime in the Crystallization of Lysozyme. *Cryst. Growth Des.* **2018**, *18*, 1483−1494.

(21) Guo, C.; Wang, J.; Li, J.; Wang, Z.; Tang, S. Kinetic Pathways and Mechanisms of Two-Step Nucleation in Crystallization. *J. Phys. Chem. Lett.* **2016**, *7*, 5008−5014.

(22) Hsieh, M.-C.; Lynn, D. G.; Grover, M. A. Kinetic Model for Two-Step Nucleation of Peptide Assembly. *J. Phys. Chem. B* **2017**, *B121*, 7401−7411.

(23) Matsarskaia, O.; Roosen-Runge, F.; Lotze, G.; Möller, J.; Mariani, A.; Zhang, F.; Schreiber, F. Tuning Phase Transitions of Aqueous Protein Solutions by Multivalent Cations. *Phys. Chem. Chem. Phys.* **2018**, *20*, 27214−27225.

(24) Braun, M. K.; Sauter, A.; Matsarskaia, O.; Wolf, M.; Roosen-Runge, F.; Sztucki, M.; Roth, R.; Zhang, F.; Schreiber, F. Reentrant Phase Behavior in Protein Solutions Induced by Multivalent Salts: Strong Effect of Anions Cl^- Versus NO_3^-. *J. Phys. Chem. B* **2018**, *B122*, 11978−11985.

(25) Luft, J. R.; Wolfley, J. R.; Said, M. I.; Nagel, R. M.; Lauricella, A. M.; Smith, J. L.; Thayer, M. H.; Veatch, C. K.; Snell, E. H.; Malkowski, M. G.; DeTitta, G. T. Efficient Optimization of Crystallization Conditions by Manipulation of Drop Volume Ratio and Temperature. *Protein Sci.* **2007**, *16*, 715−722.

(26) Matsarskaia, O.; Braun, M. K.; Roosen-Runge, F.; Wolf, M.; Zhang, F.; Roth, R.; Schreiber, F. Cation-Induced Hydration Effects Cause Lower Critical Solution Temperature Behavior in Protein Solutions. *J. Phys. Chem. B* **2016**, *B120*, 7731−7736.

(27) Zhang, C.-Y.; Liu, Y.; Tian, X.-H.; Liu, W.-J.; Li, X.-Y.; Yang, L.-X.; Jiang, H.-J.; Han, C.; Chen, K.-A.; Yin, D.-C. Effect of Real-World Sounds on Protein Crystallization. *Int. J. Biol. Macromol.* **2018**, *112*, 841−851.

(28) Guo, S.; Pranantyo, D.; Kang, E.-T.; Loh, X. J.; Zhu, X.; Janczewski, D.; Neoh, K. G. Dominant Albumin-Surface Interactions under Independent Control of Surface Charge and Wettability. *Langmuir* **2018**, *34*, 1953−1966.

DOI: 10.1021/acs.cgd.9b00858
Cryst. Growth Des. 2019, 19, 7036−7045

(29) Koizumi, H.; Uda, S.; Tsukamoto, K.; Tachibana, M.; Kojima, K.; Okada, J.; Nozawa, J. Crystallization Technique of High-Quality Protein Crystals Controlling Surface Free Energy. *Cryst. Growth Des.* **2017**, *17*, 6712−6718.
(30) Braun, M. K.; Wolf, M.; Matsarskaia, O.; Da Vela, S.; Roosen-Runge, F.; Sztucki, M.; Roth, R.; Zhang, F.; Schreiber, F. Strong Isotope Effects on Effective Interactions and Phase Behavior in Protein Solutions in the Presence of Multivalent Ions. *J. Phys. Chem. B* **2017**, *B121*, 1731−1739.
(31) Bucciarelli, S.; Mahmoudi, N.; Casal-Dujat, L.; Jehannin, M.; Jud, C.; Stradner, A. Extended Law of Corresponding States Applied to Solvent Isotope Effect on a Globular Protein. *J. Phys. Chem. Lett.* **2016**, *7*, 1610−1615.
(32) Lu, J.; Wang, X.-J.; Ching, C.-B. Batch Crystallization of Soluble Proteins: Effect of Precipitant, Temperature and Additive. *Prog. Cryst. Growth Charact. Mater.* **2002**, *45*, 201−217.
(33) Gögelein, C.; Wagner, D.; Cardinaux, F.; Nägele, G.; Egelhaaf, S. U. Effect of glycerol and dimethyl sulfoxide on the phase behavior of lysozyme: Theory and experiments. *J. Chem. Phys.* **2012**, *136*, 015102.
(34) Nanev, C. N. Recent Insights into the Crystallization Process; Protein Crystal Nucleation and Growth Peculiarities; Processes in the Presence of Electric Fields. *Crystals* **2017**, *7*, 310.
(35) Zhang, F. Nonclassical Nucleation Pathways in Protein Crystallization. *J. Phys.: Condens. Matter* **2017**, *29*, 443002.
(36) Zhang, Y.; Zhao, J.; Di, J.; Jiang, H.; Wang, Q.; Wang, J.; Guo, Y.; Yin, D. Real-Time Monitoring of the Solution Concentration Variation During the Crystallization Process of Protein-Lysozyme by Using Digital Holographic Interferometry. *Opt. Express* **2012**, *20*, 18415−18421.
(37) Nakamura, A.; Ohtsuka, J.; Kashiwagi, T.; Numoto, N.; Hirota, N.; Ode, T.; Okada, H.; Nagata, K.; Kiyohara, M.; Suzuki, E.-i.; Kita, A.; Wada, H.; Tanokura, M. In-Situ and Real-Time Growth Observation of High-Quality Protein Crystals Under Quasi-Microgravity on Earth. *Sci. Rep.* **2016**, *6*, 22127.
(38) Tsarfati, Y.; Rosenne, S.; Weissman, H.; Shimon, L. J. W.; Gur, D.; Palmer, B. A.; Rybtchinski, B. Crystallization of Organic Molecules: Nonclassical Mechanism Revealed by Direct Imaging. *ACS Cent. Sci.* **2018**, *4*, 1031−1036.
(39) Vekilov, P. G. Dense Liquid Precursor for the Nucleation of Ordered Solid Phases from Solution. *Cryst. Growth Des.* **2004**, *4*, 671−685.
(40) Duff, M. R.; Borreguero, J. M.; Cuneo, M. J.; Ramanathan, A.; He, J.; Kamath, G.; Chennubhotla, S. C.; Meilleur, F.; Howell, E. E.; Herwig, K. W.; Myles, D. A. A.; Agarwal, P. K. Modulating Enzyme Activity by Altering Protein Dynamics with Solvent. *Biochemistry* **2018**, *57*, 4263−4275.
(41) Porcar, L.; Falus, P.; Chen, W.-R.; Faraone, A.; Fratini, E.; Hong, K.; Baglioni, P.; Liu, Y. Formation of the Dynamic Clusters in Concentrated Lysozyme Protein Solutions. *J. Phys. Chem. Lett.* **2010**, *1*, 126−129.
(42) Braun, M. K.; Grimaldo, M.; Roosen-Runge, F.; Hoffmann, I.; Czakkel, O.; Sztucki, M.; Zhang, F.; Schreiber, F.; Seydel, T. Crowding-Controlled Cluster Size in Concentrated Aqueous Protein Solutions: Structure, Self- and Collective Diffusion. *J. Phys. Chem. Lett.* **2017**, *8*, 2590−2596.
(43) Grimaldo, M.; Roosen-Runge, F.; Zhang, F.; Seydel, T.; Schreiber, F. Diffusion and Dynamics of γ-Globulin in Crowded Aqueous Solutions. *J. Phys. Chem. B* **2014**, *B118*, 7203−7209.
(44) Grimaldo, M.; Roosen-Runge, F.; Hennig, M.; Zanini, F.; Zhang, F.; Zamponi, M.; Jalarvo, N.; Schreiber, F.; Seydel, T. Salt-Induced Universal Slowing Down of the Short-Time Self-Diffusion of a Globular Protein in Aqueous Solution. *J. Phys. Chem. Lett.* **2015**, *6*, 2577−2582.
(45) Grimaldo, M.; Roosen-Runge, F.; Hennig, M.; Zanini, F.; Zhang, F.; Jalarvo, N.; Zamponi, M.; Schreiber, F.; Seydel, T. Hierarchical Molecular Dynamics of Bovine Serum Albumin in Concentrated Aqueous Solution Below and Above Thermal Denaturation. *Phys. Chem. Chem. Phys.* **2015**, *17*, 4645−4655.
(46) Roosen-Runge, F.; Hennig, M.; Zhang, F.; Jacobs, R. M. J.; Sztucki, M.; Schober, H.; Seydel, T.; Schreiber, F. Protein Self-Diffusion in Crowded Solutions. *Proc. Natl. Acad. Sci. U. S. A.* **2011**, *108*, 11815−11820.
(47) Beck, C.; Grimaldo, M.; Roosen-Runge, F.; Braun, M. K.; Zhang, F.; Schreiber, F.; Seydel, T. Nanosecond Tracer Diffusion as a Probe of the Solution Structure and Molecular Mobility of Protein Assemblies: The Case of Ovalbumin. *J. Phys. Chem. B* **2018**, *B122*, 8343−8350.
(48) Anunciado, D. B.; Nyugen, V. P.; Hurst, G. B.; Doktycz, M. J.; Urban, V.; Langan, P.; Mamontov, E.; O'Neill, H. In Vivo Protein Dynamics on the Nanometer Length Scale and Nanosecond Time Scale. *J. Phys. Chem. Lett.* **2017**, *8*, 1899−1904.
(49) Kontopidis, G.; Holt, C.; Sawyer, L. Invited Review: β-Lactoglobulin: Binding Properties, Structure, and Function. *J. Dairy Sci.* **2004**, *87*, 785−796.
(50) Sakurai, K.; Konuma, T.; Yagi, M.; Goto, Y. Structural dynamics and folding of β-lactoglobulin probed by heteronuclear NMR. *Biochim. Biophys. Acta, Gen. Subj.* **2009**, *1790*, 527−537 Recent Advances in Biochemistry, Biophysics and Molecular Biology..
(51) Grimaldo, M.; Roosen-Runge, F.; Zhang, F.; Schreiber, F.; Seydel, T. Dynamics of proteins in solution. *Q. Rev. Biophys.* **2019**, *52*, No. e7.
(52) Lieutenant, K.; Lindner, P.; Gahler, R. A New Design for the Standard Pinhole Small-Angle Neutron Scattering Instrument D11. *J. Appl. Crystallogr.* **2007**, *40*, 1056−1063.
(53) Zhang, F.; Braun, M.; Da Vela, S.; Grimaldo, M.; Matsarskaia, O.; Roosen-Runge, F.; Schreiber, F.; Schweins, R.; Seydel, T.; Benedikt, S. *Kinetics of Two-Step Nucleation in Protein Crystallization Studied by Real-Time SANS*; Institut Laue-Langevin (ILL), 2015; DOI: 10.5291/ILL-DATA.9-13-620.
(54) Grimaldo, M.; Beck, C.; Braun, M.; Czakkel, O.; Roosen-Runge, F.; Sauter, A.; Schreiber, F.; Seydel, T.; Zhang, F. *Real Time Study of Protein Dynamics during a One-Step and a Two-Step Crystallization Process*; Institut Laue-Langevin (ILL), 2015; DOI: 10.5291/ILL-DATA.-−04-760.
(55) Frick, B.; Mamontov, E.; Eijck, L. V.; Seydel, T. Recent Backscattering Instrument Developments at the ILL and SNS. *Z. Phys. Chem.* **2010**, *224*, 33−60.
(56) Hennig, M.; Frick, B.; Seydel, T. Optimum Velocity of a Phase-Space Transformer for Cold-Neutron Backscattering Spectroscopy. *J. Appl. Crystallogr.* **2011**, *44*, 467−472.
(57) Farago, B. Recent Neutron Spin-Echo Developments at the ILL (IN11 and IN15). *Phys. B (Amsterdam, Neth.)* **1999**, *267−268*, 270−276.
(58) Squires, G. L. *Introduction to the Theory of Thermal Neutron Scattering*, 3rd ed.; Cambridge University Press, 2012.
(59) Soraruf, D.; Roosen-Runge, F.; Grimaldo, M.; Zanini, F.; Schweins, R.; Seydel, T.; Zhang, F.; Roth, R.; Oettel, M.; Schreiber, F. Protein Cluster Formation in Aqueous Solution in the Presence of Multivalent Metal Ions - A Light Scattering Study. *Soft Matter* **2014**, *10*, 894−902.
(60) Frontzek, A. V.; Paccou, L.; Guinet, Y.; Hédoux, A. Study of the Phase Transition in Lysozyme Crystals by Raman Spectroscopy. *Biochim. Biophys. Acta, Gen. Subj.* **2016**, *1860*, 412−423.
(61) Reif, B.; Xue, Y.; Agarwal, V.; Pavlova, M. S.; Hologne, M.; Diehl, A.; Ryabov, Y. E.; Skrynnikov, N. R. Protein Side-Chain Dynamics Observed by Solution-and Solid-State NMR: Comparative Analysis of Methyl ^{2}H Relaxation Data. *J. Am. Chem. Soc.* **2006**, *128*, 12354−12355.
(62) Agarwal, V.; Xue, Y.; Reif, B.; Skrynnikov, N. R. Protein Side-Chain Dynamics As Observed by Solution-and Solid-State NMR Spectroscopy: A Similarity Revealed. *J. Am. Chem. Soc.* **2008**, *130*, 16611−16621.
(63) Bée, M. A Physical Insight Into the Elastic Incoherent Structure Factor. *Phys. B* **1992**, *B182*, 323−336.
(64) Grimaldo, M.; Roosen-Runge, F.; Jalarvo, N.; Zamponi, M.; Zanini, F.; Hennig, M.; Zhang, F.; Schreiber, F.; Seydel, T. High-

DOI: 10.1021/acs.cgd.9b00858
Cryst. Growth Des. 2019, 19, 7036−7045

Resolution Neutron Spectroscopy on Protein Solution Samples. *EPJ Web Conf.* **2015**, *83*, 02005.
(65) Singwi, K. S.; Sjölander, A. Diffusive Motions in Water and Cold Neutron Scattering. *Phys. Rev.* **1960**, *119*, 863−871.
(66) Martin, W. G.; Winkler, C. A.; Cook, W. H. Partial Specific Volume Measurements by Differential Sedimentation. *Can. J. Chem.* **1959**, *37*, 1662−1670.

DOI: 10.1021/acs.cgd.9b00858
Cryst. Growth Des. 2019, 19, 7036−7045